Dalton Transactions

ROYAL SOCIETY OF CHEMISTRY

PAPER

View Article Online
View Journal | View Issue

Cite this: *Dalton Trans.*, 2025, **54**, 9261

Dimensionality-driven photoluminescence enhancement in Cl/Br mixed-halide organic–inorganic hybrid cadmium halides†

Boyoung Kim and Kang Min Ok *

Received 17th April 2025,
Accepted 14th May 2025

DOI: 10.1039/d5dt00908a

rsc.li/dalton

In this study, we report the successful synthesis of four organic–inorganic hybrid materials by systematically varying the Cl/Br halide ratio in a system comprising 4-(2-ammonioethyl)pyridinium organic cations and cadmium halides. An increase in Cl content induces a structural transition from zero-dimensional to two-dimensional (2D) frameworks, with the 2D phase featuring a unique corrugated layered architecture composed of corner-, edge-, and face-sharing Cd-halide octahedra. All compounds exhibit broadband blue photoluminescence, and a clear correlation is observed between halide mixing, increased structural distortion, and enhanced photoluminescence quantum yield (PLQY). Notably, the PLQY increases significantly from 6% to 36% in the 2D mixed halide compound. These findings underscore the effectiveness of halide composition modulation in tuning both structural dimensionality and optical performance, providing valuable insights for the rational design of high-efficiency luminescence materials.

Introduction

Organic–inorganic hybrid metal halides (OIMHs) have emerged as promising materials for a wide range of optoelectronic applications, including energy storage devices, perovskite solar cells, light-emitting diodes, and sensors.[1–6] Their appeal lies in their unique optoelectronic properties, low-cost and scalable synthesis, and high structural and compositional tunability.

One of the most attractive features of OIMHs is their structural dimensionality, which can range from zero-dimensional (0D) to one-dimensional (1D), two-dimensional (2D), and three-dimensional (3D) frameworks. These dimensional variations significantly influence their optical, electrical, and thermal properties. While 3D perovskites are known for their excellent carrier mobility and strong light absorption, their poor environmental stability remains a major drawback.[7] In contrast, low-dimensional OIMHs exhibit enhanced thermal and moisture stability, greater structural flexibility, and superior photoluminescence (PL) performance, attributable to strong quantum confinement effects and high exciton binding energies.[8–10] Owing to the close correlation between structural dimensionality and PL properties, numerous studies have focused on precisely tuning emission characteristics—such as emission wavelength and photoluminescence quantum yield (PLQY)—through structural control.[11–14]

In particular, 2D OIMHs possess a quantum well-like architecture, in which inorganic layers are separated by organic cations, giving rise to strong exciton binding energies.[15,16] Most 2D OIMHs exhibit (100)-oriented layered structures composed of corner-sharing metal–halide octahedra. However, structural distortions induced by bulky or asymmetric organic cations can lead to corrugated networks that deviate from ideal flat layers.[17,18] In some cases, mixed connectivity involving edge-sharing and face-sharing octahedra has also been observed. For example, $(H_2Aepz)_2Pb_4I_{14}$[19] and $[DAPMA]_2Pb_3X_{12}{\cdot}2H_2O$ (X = Cl, Br)[20] adopt structures in which PbX_6 octahedra are connected *via* both edge- and corner-sharing. Similarly, in cadmium-based 2D halide systems, $[CdX_6]$ octahedra typically form $[CdX_4]^{2-}$ layered anionic frameworks,[21–23] although in rarer cases, 2D $[Cd_3Cl_{10}]^{4-}$ networks composed of corner- and face-sharing octahedra have been reported.[24,25] These variations in octahedral connectivity significantly influence the electronic structures and photophysical properties of the materials.[26,27] Thus, the diverse topologies available in low-dimensional OIMHs provide a powerful platform for rational design and fine-tuning of functional properties.

The compositional flexibility of OIMHs-enabled by the vast array of available organic cations, central metal cations, and halide anions-further expands the design space.[28,29,30] Among

Department of Chemistry, Sogang University, Seoul 04107, Republic of Korea. E-mail: kmok@sogang.ac.kr

†Electronic supplementary information (ESI) available: Crystallographic data, halogen weight percentages and atomic ratios, distortion values, PXRD patterns, TGA diagrams, UV-vis-diffuse reflectance spectra, IR spectra, EDS spectra, band structures, DOS for the reported compounds. CCDC 2444367–2444370. For ESI and crystallographic data in CIF or other electronic format see DOI: https://doi.org/10.1039/d5dt00908a

the various strategies for property modulation, halogen substitution stands out as particularly effective. For instance, incorporating halogen atoms into organic cations can induce permanent dipoles and increase structural asymmetry and polarity.[31,32] Meanwhile, substitution or mixing of halide anions within the inorganic framework has been shown to tune key material properties such as phase transition temperature, emission wavelength, optical bandgap, and PLQY.[33–37] These strategies have led to the development of customized OIMHs with multifunctional performance.

In this study, we report four halide-regulated cadmium-based OIMHs-(4AEP)$CdBr_4$ (pure Br), (4AEP)$CdBr_2Cl_2$ (Cl 50%), $(4AEP)_4Cd_5Br_4Cl_{14}$ (Cl 80%), and $(4AEP)_4Cd_5Cl_{18}$ (pure Cl or Cl 100%)-synthesized using 4-(2-ammonioethyl)pyridinium [$(4AEP)^{2+}$] as the organic cation and various Br/Cl mixed halides. By systematically tuning the Br/Cl ratio, we achieve a dimensional transformation from isolated 0D tetrahedral units to 2D layered structures. All compounds exhibit broadband blue emission, with PLQY showing a remarkable enhancement upon halide mixing. In particular, the 2D Cl 80% compound exhibits a PLQY of 36%, representing a six-fold increase compared to the Cl 100% phase. Although high-PLQY materials such as DMP-1-$CdBr_3$ (52%)[14] and $(H_2AMP)CdBr_4{\cdot}H_2O$ (23.5%)[38] have been reported, most Cd-based OIMHs typically exhibit PLQYs below 10%.[39–42] Compared to these conventional Cd-based OIMHs, the Cl 80% compound demonstrates superior PLQY, highlighting the synergistic effect of dimensionality control and halide composition in enhancing the optical performance of OIMHs.

Experimental

Reagents

$CdCl_2{\cdot}2.5H_2O$ (98%, Kanto Chemical Co., Inc.), $CdBr_2{\cdot}4H_2O$ (99%, Alfa Aesar), 4-(2-aminoethyl)pyridine (97%, TCI), HBr (47.0–49.0%, Daejung), HCl (35.0–37.0 wt%, Samchun), isopropanol (99.5%, Daejung), and ethanol (99.9%, Samchun) were used as received without further purification.

Synthesis

All compounds were synthesized *via* the antisolvent crystallization method. The reaction solutions were prepared as follows. For the Cl 100% compound, 1 mmol of $CdCl_2{\cdot}2.5H_2O$ (0.232 g) and 0.8 mmol of 4AEP (100 μL) were dissolved in a mixture of 0.2 mL HCl and 3 mL deionized water. For the Cl 80% compound, 1 mmol of $CdBr_2{\cdot}4H_2O$ (0.347 g) and 0.8 mmol of 4AEP were dissolved in 0.5 mL HCl and 3 mL deionized water. For the Cl 50% compound, 0.8 mmol of $CdBr_2{\cdot}4H_2O$ (0.296 g) and 4AEP were dissolved in 0.17 mL HCl and 3 mL deionized water. For the pure Br compound, 0.8 mmol of $CdBr_2{\cdot}4H_2O$ and 4AEP were dissolved in a mixture of 0.33 mL HBr and 3 mL deionized water. Each solution was stirred until clear, followed by the dropwise addition of ethanol (for Cl 100%) or isopropanol (IPA) (for others) until turbidity was observed. The resulting cloudy solutions were then heated to 60 °C until clear and subsequently cooled slowly to room temperature to induce crystallization. The crystals were collected by vacuum filtration and washed with ethanol (Cl 100%) or IPA (others). Block-shaped crystals were obtained for the Cl 50% compound, while plate-shaped crystals formed for the Cl 80%, Cl 100%, and pure Br compounds. The isolated yields were 0.273 g (69%) for Cl 100%, 0.211 g (59%) for Cl 80%, 0.298 g (76%) for Cl 50%, and 0.361 g (77%) for the pure Br compound.

Single-crystal X-ray diffraction (SC-XRD)

SC-XRD data for all materials were collected using a Bruker D8 QUEST diffractometer equipped with a graphite-monochromated Mo Kα radiation source (λ = 0.71073 Å) at room temperature, at the Advanced Bio-Interface Core Research Facility, Sogang University. Data processing was performed using APEX5. Integration and absorption corrections were applied using the SAINT[43] and SADABS[44] programs. The crystal structures were solved and refined using SHELXT-2015[45] and SHELXL-2015[46] within the WinGX-2014[47] program suite. Detailed crystallographic data are summarized in Table S1.†

Powder X-ray diffraction (PXRD)

PXRD patterns were recorded on a Rigaku MiniFlex 600 diffractometer using Cu Kα radiation (λ = 1.5406 Å) at room temperature. Scans were conducted over a 2θ range of 5–70° with a step size of 0.02° and a scan speed of 20° min^{-1}. The experimental PXRD patterns show good agreement with the simulated patterns generated from the SC-XRD data.

Thermogravimetric analysis (TGA)

TGA measurements were carried out using a SCINCO TGA-N 1000 thermal analyzer. Polycrystalline samples were heated in alumina crucibles from 25 °C to 900 °C at a rate of 10 °C min^{-1} under an air flow.

Ultraviolet–visible (UV–vis) diffuse reflectance spectroscopy

UV-vis diffuse reflectance spectra were acquired using a Jasco V-660 spectrophotometer equipped with a Jasco V-720 accessory. Band gap energies were estimated using the Kubelka–Munk function applied to the reflectance data.

Infrared (IR) spectroscopy

IR spectra were obtained using a Thermo Scientific Nicolet iS50 FT-IR spectrometer equipped with an attenuated total reflection accessory, over the range of 550 to 4000 cm^{-1}.

Photoluminescence (PL) spectroscopy

Solid-state PL spectra were recorded using a Jasco FP-8550 spectrofluorometer with a xenon lamp. All measurements were performed on polycrystalline samples. Photoluminescence quantum yields (PLQYs) were measured using an integrating sphere (JASCO ILF-135) connected to the spectrofluorometer.

Elemental analysis

Elemental composition and surface distribution were analyzed using energy-dispersive X-ray spectroscopy (EDS) mode on a field-emission scanning electron microscope (JSM-7100 F). The Br/Cl ratios in mixed halide samples were quantified by ion chromatography (Yanaco, YHS-11). Elemental analysis for C, H, and N was performed using Thermo Flash 2000/Flash EA1112 analyzers.

Computational calculations

Electronic structure calculations were performed using a plane-wave pseudopotential approach based on density functional theory (DFT), as implemented in the CASTEP[48] package. Band structures and densities of states were calculated using the Perdew–Burke–Ernzerhof functional within the generalized gradient approximation. A plane-wave cutoff energy of 830 eV was used. The *k*-point grids were set to 5 × 4 × 3 for pure Br and Cl 50%, and 4 × 3 × 2 for Cl 80% and 100%. The following valence electrons were included: Cd $5s^2 4d^{10}$, Br $4s^2 4p^5$, Cl $3s^2 3p^5$, C $2s^2 2p^2$, N $2s^2 2p^3$, H $1s^1$.

Results and discussion

Crystal structures

The pure Br phase, (4AEP)$CdBr_4$, crystallizes in the centrosymmetric space group, $P2_1/c$ (Fig. 1a). Its structure features a 0D configuration, where $[CdBr_4]^{2-}$ tetrahedral monomers are aligned along the *a*-axis and interact with 4AEP through hydrogen bonding. These hydrogen bonds form between either the N–H group of the pyridinium ring or the N–H of the NH_3^+ group and the Br atoms of $[CdBr_4]^{2-}$, with bond lengths ranging from 2.47 to 3.12 Å (Table S6 and Fig. S13†).

Upon partial substitution of Br with Cl, the crystallographic symmetry changes, leading to structural variations that depend on the Cl content (Table S1†). Cl atoms are randomly incorporated at Br sites, inducing a symmetry transition from $P2_1/c$ to $P\bar{1}$ (Fig. 1b). The structure of (4AEP)$CdBr_2Cl_2$ corresponding to 50% Cl substitution, was determined by SC-XRD, and the Br/Cl ratio was confirmed *via* EDS and halogen ion chromatography (Table S14 and Fig. S6–S9†). Similar to the pure Br phase, the Cl 50% structure consists of $[CdBr_{4-x}Cl_x]^{2-}$ tetrahedral monomers, which form hydrogen bonds with $(4AEP)^{2+}$ in the range of 2.47–3.04 Å, resulting in a 0D framework (Table S7†).

Detailed analysis of the extended structures of the pure Br and Cl 50% compounds reveals key differences. As shown in Fig. 2a and d, the Cd-X tetrahedra are linearly arranged along the *a*-axis, while the pyridine rings of $(4AEP)^{2+}$ stack along the *c*-axis and *b*-axis, respectively. The interplanar distances between the stacked rings are 3.67 Å and 3.83 Å, respectively. However, the centroid-to-centroid distances are 5.27 Å and 4.77 Å, suggesting the presence of weak π–π interactions. Fig. 2b and c highlight the conformational differences of the $(4AEP)^{2+}$ ligands: in the pure Br compound, the aminoethyl group is nearly parallel to the pyridine ring, whereas in the Cl 50% compound, it adopts a nearly perpendicular orientation (approximately 90°). This conformational change arises from Cl substitution. As the more electronegative Cl atoms substitute Br, the strength of hydrogen bonding with $(4AEP)^{2+}$

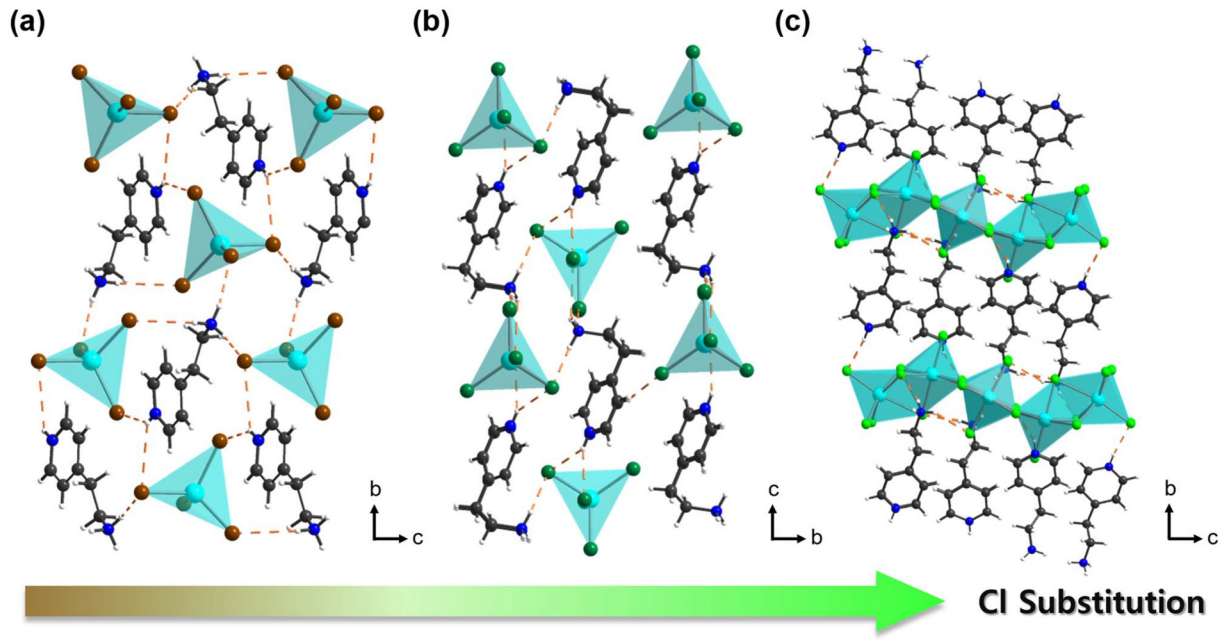

Fig. 1 Ball-and-stick and polyhedral representations of the crystal structures of (a) pure Br phase, (4AEP)$CdBr_4$; (b) Cl 50% phase, (4AEP)$CdBr_2Cl_2$; and (c) pure Cl phase, $(4AEP)_4Cd_5Cl_{18}$ (cyan, Cd; brown, Br; green, Br/Cl; light green, Cl; black, C; blue, N; white, H; orange dashed line, hydrogen bond).

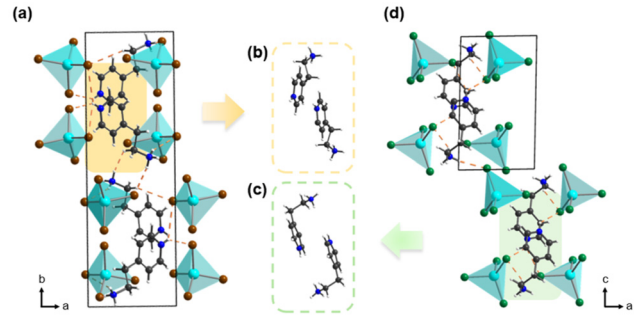

Fig. 2 Ball-and-stick and polyhedral representations of (a) the crystal structure of the pure Br compound, viewed along the *ab*-plane; and the interaction and arrangement of $(4AEP)^{2+}$ in (b) the pure Br compound, $(4AEP)CdBr_4$, and (c) the Cl 50% compound, $(4AEP)CdBr_2Cl_2$. (d) Crystal structure of the Cl 50% compound viewed along the *ac*-plane (cyan, Cd; brown, Br; green, Br/Cl; black, C; blue, N; white, H; orange dashed line, hydrogen bond).

increases, resulting in shorter hydrogen bond lengths and a decrease in Cd–X bond lengths from 2.58–2.60 Å to 2.51–2.57 Å (Tables S2 and S3†).

As the Cl ratio increases, a significant structural transformation occurs-from a 0D structure to a 2D structure (Fig. 1). The Cl-rich phase $(4AEP)_4Cd_5Br_{18-x}Cl_x$ (≥70% Cl) also crystallizes in the space group, $P\bar{1}$. PXRD patterns show a progressive peak shift with increasing Br content, indicating an expansion of the unit cell (Fig. S2b†).

In this structure, $[CdBr_{6-x}Cl_x]$ octahedra form extended $[Cd_5Br_{18-x}Cl_x]$ layers, which adopt a previously unreported unique arrangement composed of face-sharing, edge-sharing, and corner-sharing octahedra (Fig. 3a and b). Specifically, a $[Cd_5Cl_{18}]^{8-}$ layer, assembled through face- and edge-sharing connections, is corner-shared with two $[CdCl_6]^{4-}$ octahedra. This connectivity results in an extended framework containing 4- (4-MRs) and 10-membered rings (10-MRs) (Fig. 3c). Owing to the rigidity imposed by face-sharing interactions, the resulting layer is not flat but adopts a 'wave-like' (corrugated) conformation.[18,19,26,49,50]

In the interlayer region, hydrogen bonding occurs between the N–H groups of the pyridinium ring or the NH_3^+ moiety and the Br/Cl atoms of the $[Cd_5Br_{18-x}Cl_x]^{8-}$ layers. The hydrogen bond lengths range from 2.28 to 2.92 Å in the pure Cl phase and from 2.40 to 3.11 Å in the Cl 80% phase (Tables S8 and S9†). The N–H group of the pyridinium ring forms a single hydrogen bond with the layer, whereas the NH_3^+ group participates in multiple hydrogen bonds within the 4-MRs and 10-MRs (Fig. S14†).

The combined face-, edge-, and corner-sharing interactions impose structural constraints, making it energetically less favorable to maintain the layered architecture as the proportion of the relatively larger Br atoms increases. As a result, the simpler and more stable 0D structure is preferred at higher Br contents. Furthermore, the mixture of these bonding modes leads to an increase in the distortion values (Δd) of the Cd-centered octahedra, from 1.156×10^{-5} to 2.891×10^{-3} compared to the 0D structure. Among the Cd centers, Cd(1)-involved in both face- and edge-sharing-exhibits the highest distortion.

Additionally, the incorporation of mixed Br/Cl introduces further distortions in both octahedral and tetrahedral units due to the difference in Cd–Br and Cd–Cl bond lengths. In the

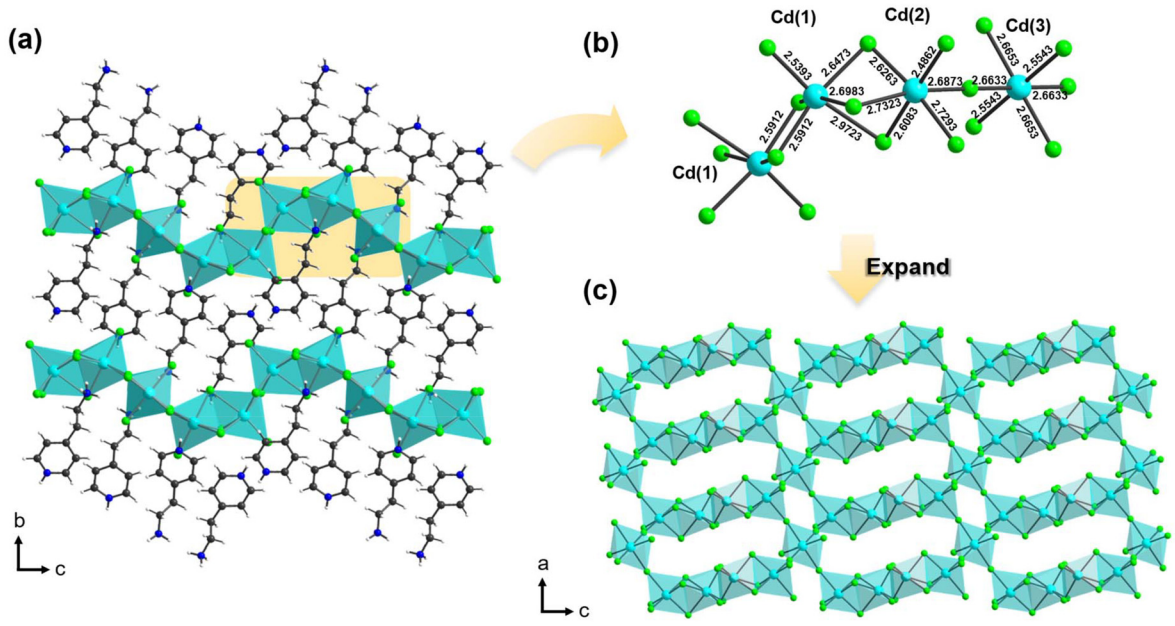

Fig. 3 Ball-and-stick and polyhedral representations of (a) the pure Cl phase, $(4AEP)_4Cd_5Cl_{18}$; (b) illustration of face-, edge-, and corner-sharing octahedra; and (c) the extended $[Cd_5Cl_{18}]^{8-}$ layer (cyan, Cd; light green, Cl; black, C; blue, N; white, H; orange dashed line, hydrogen bond).

0D structures, the distortion values increase from 1.156×10^{-5} to 1.017×10^{-4}, while in the 2D structure, they rise from 2.891×10^{-3} to 3.054×10^{-3} (Table S15†).

IR spectroscopy

The functional groups in the compounds were identified by IR spectroscopy. The band in the 3200–3100 cm^{-1} region corresponds to N–H stretching vibrations. Strong hydrogen bonding with cadmium halides weakens these vibrations, resulting in a red shift. The 3000–3090 cm^{-1} region is attributed to C–H stretching vibrations of the pyridine ring. Peaks in the 1070–1130 cm^{-1} and around 800 cm^{-1} regions correspond to in-plane and out-of-plane bending vibrations, respectively. In the 1650–1450 cm^{-1} range, overlapping peaks arise from pyridine ring (C–C, C–N) stretching and N–H bending vibrations. The C–N stretching vibration is observed in the 1200–1248 cm^{-1} region (Fig. S5†).

UV-vis diffuse reflectance spectroscopy

The diffuse reflectance spectra of all compounds show UV cut-off edges at *ca.* 270 nm and a broad absorption peak around 400 nm, which corresponds to the slight yellowish tint of the powdered samples (Fig. S4†). The optical band gaps, calculated using the Kubelka–Munk function, are 4.16, 4.25, 4.13, and 4.36 eV for Cl ratios of 0%, 50%, 80%, and 100%, respectively. Although no clear trend is observed across all four compounds due to structural variations, a higher Cl content is associated with larger optical band gaps in both structurally similar pairs-pure Br and Cl 50%, and Cl 80% and pure Cl. These observations suggest that both the crystal structure and Cl/Br ratio significantly influence the optical band gap (Fig. S4†).

Density of states and band structures

The band structures and density of states (DOS) were investigated using DFT calculations. The calculated band gaps are *ca.* 2.88, 3.03, 2.92, and 3.13 eV for the pure Br phase, Cl 50%, Cl 80%, and pure Cl (100%) phases, respectively (Fig. S10†). These values are smaller than the experimental band gaps, which is commonly observed due to the limitations of the exchange–correlation function in standard DFT.

The DOS plots provide insight into the electronic structures of the compounds. For the pure Cl compound, the valence band maximum (VBM) is primarily composed of Cl 3p orbitals, while the conduction band minimum (CBM) originates mainly from C 2p and N 2p orbitals. Similarly, in the pure Br phase, the VBM is derived from Br 4p orbitals, and the CBM is dominated by C 2p and N 2p orbitals. In the mixed Cl/Br compounds, the VBM consists of a combination of Cl 3p and Br 4p orbitals, while the CBM remains primarily composed of C 2p and N 2p orbitals. These features are consistent across all compounds regardless of halide composition, indicating that both halide and ligand orbitals play a crucial role in band gap formation. Furthermore, within the isostructural 2D structures (Cl 100% to Cl 80%), an increase in Br content (and corresponding decrease in Cl) results in a reduced band gap, which correlates with observed changes in PL behavior (Fig. S11†).

Stability in organic solvents and water

The stability of the Cl-rich compound with a 2D structure was evaluated in water and various organic solvents. Owing to its high-water solubility, the compound dissolved and recrystallized *via* slow evaporation. For organic solvents, the sample was immersed for three days, and its stability was assessed *via* PXRD. The resulting PXRD patterns confirm the retention of crystallinity, indicating that the Cl-rich compound does not decompose in water or the tested organic solvents (Fig. S12†).

Thermal stability

According to TGA analysis, all compounds exhibited thermal stability above approximately 200 °C. In particular, the pure Cl- and Br-based compounds remained stable up to around 230 °C, whereas the Cl/Br mixed-halide compounds began to decompose at approximately 200 °C. This suggests that pure halide compounds exhibit greater thermal stability than their mixed-halide counterparts, and that the disordered incorporation of Cl and Br may compromise the thermal stability of the crystal structure. Additionally, all four compounds exhibited a sharp weight loss of around 30% in the TGA curves. Based on the theoretical weight percentages of $(4AEP)^{2+}$ in the pure Cl, Cl 80%, Cl 50%, and pure Br compounds—calculated as 29.3%, 26.5%, 26.6%, and 22.3%, respectively—it can be inferred that the organic cation $(4AEP)^{2+}$ is released first from the structure during thermal decomposition (Fig. S3†).

PL spectroscopy

Pure Br, Cl 50%, Cl 80%, and pure Cl exhibit maximum broadband emission peaks at 430 nm, 408 nm, 472 nm, and 419 nm, respectively, when excited at 280 nm, 370 nm, 275 nm, and 370 nm. All samples display blue emission. However, no clear trend in emission wavelength is observed with respect to the Br/Cl ratio due to the substantial structural differences between the 0D and 2D structures. The pure Br and Cl 80% compounds exhibit large Stokes shifts of 150 nm and 197 nm, respectively, with full width at half maximum of 105 nm and 111 nm. Despite the large Stokes shifts and broadband emission profiles, all compounds consistently exhibit blue emission. These features are attributed commonly observed in cadmium halide hybrid materials and are attributed to radiative recombination *via* self-trapped excitons (STEs) (Fig. 4a).[39,40,51,52]

In Cl-rich materials with consistent 2D structural frameworks, Br substitution leads to a reduction in the bandgap, resulting in a red shift of the emission wavelength upon excitation at 275 nm. In addition, a significant enhancement in PL intensity is observed in Cl 80% compared to pure Cl (Fig. 4b and c). This intensity difference aligns with the PLQY results. The measured PLQY values are 4.93%, 7.91%, 35.88%, and 5.91% for pure Br, Cl 50%, Cl 80%, and pure Cl, respectively (Fig. 4d).

When the composition changes from Cl 100% to Cl 80%, the PLQY increases from approximately 6% to 36%, representing a sixfold enhancement. This represents a relatively high

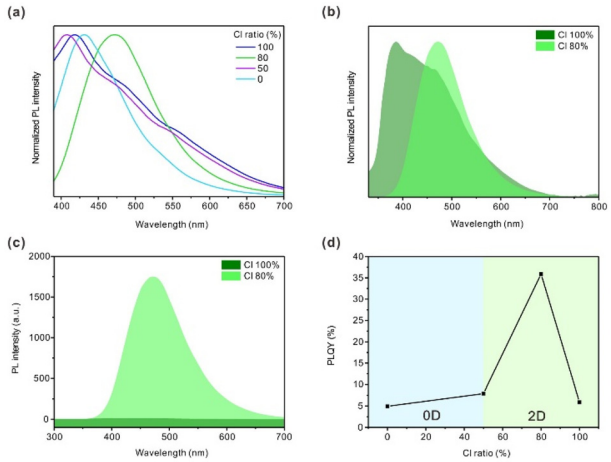

Fig. 4 (a) Normalized PL spectra for pure Br, Cl 50%, Cl 80%, and pure Cl compounds. (b) Normalized PL spectra at λ_{ex} = 275 nm for Cl ratios of 80% and 100%. (c) PL spectra at λ_{ex} = 275 nm for Cl ratios of 80% and 100%, measured at an operating voltage of 200 V. (d) Variation of PLQY with Cl ratio and structural dimensionality.

PLQY compared to typical single cadmium-based OIMHs, which generally exhibit low PLQYs of approximately 10%.[38–42] Similarly, in the 0D pure Br compound, 50% Cl substitution leads to a moderate increase in PLQY from 5% to 8%. This pronounced increase may arise from two contributing factors. First, halide mixing likely aids in defect passivation, thereby reducing nonradiative recombination pathways. This trend is generally consistent with previous reports on mixed-halide perovskite systems such as $CsPbBr_{3-x}Cl_x$, where luminescence efficiency improves as the composition shifts from $CsPbCl_3$ to $CsPbBr_3$.[53–55] Second, partial substitution of Cl^- with Br^- may introduce structural distortion in the CdX_6 octahedra (or CdX_4 tetrahedra in 0D structures), which could enhance quantum confinement and promote the formation of STEs, thereby facilitating radiative recombination. These two effects, acting in tandem, may account for the substantial increase in PLQY observed upon partial incorporation of Br^-.[56–60]

Conclusions

In this study, four organic–inorganic hybrid compounds were successfully synthesized by tuning the halide composition between Cl and Br. As the Cl ratio increased, a structural transformation from 0D to 2D was observed, with the 2D phase exhibiting a novel layered framework composed of corner-, edge-, and face-sharing octahedra. Halide mixing induced increased structural distortion, which was correlated with an enhancement in PLQY. Notably, the PLQY improved significantly from 6% to 36% in the 2D structure, demonstrating superior optical efficiency compared to typical Cd-based OIMHs, which generally exhibit PLQYs of around 10%. This work underscores the synergistic influence of halide composition and dimensionality on optical performance and provides valuable design principles for the development of high-efficiency luminescent materials.

Author contributions

K. M. O. conceived the project. B. K. conducted the experimental studies. All authors contributed to the writing and editing of the manuscript and agreed on the final version.

Data availability

The data supporting this article have been included as part of the ESI.† Crystallographic data for $(4AEP)CdBr_4$, $(4AEP)CdBr_2Cl_2$, $(4AEP)_4Cd_5Br_4Cl_{14}$, and $(4AEP)_4Cd_5Cl_{18}$ have been deposited at the CCDC under 2444367–2444370.

Conflicts of interest

There are no conflicts to declare.

Acknowledgements

This work was supported by the National Research Foundation of Korea (NRF) funded by the Ministry of Science and ICT (Grant No. RS-2024-00442105 and RS-2024-000395003). We acknowledge Prof. Eunsang Kwon at Tohoku University for assistance with the halogen ion chromatography.

References

1 K. Ding, H. Ye, C. Su, Y.-A. Xiong, G. Du, Y.-M. You, Z.-X. Zhang, S. Dong, Y. Zhang and D.-W. Fu, Superior ferroelectricity and nonlinear optical response in a hybrid germanium iodide hexagonal perovskite, *Nat. Commun.*, 2023, **14**, 2863.
2 Z. Liu, P. Cheng, R. Kang, J. Zhou, X. Wang, X. Zhao, J. Zhao, D. Liu and Z. Zuo, Piezo-Acoustic Resistive Switching Behaviors in High-Performance Organic–Inorganic Hybrid Perovskite Memristors, *Adv. Sci.*, 2024, **11**, 2308383.
3 Q. Jiang, J. Tong, Y. Xian, R. A. Kerner, S. P. Dunfield, C. Xiao, R. A. Scheidt, D. Kuciauskas, X. Wang, M. P. Hautzinger, R. Tirawat, M. C. Beard, D. P. Fenning, J. J. Berry, B. W. Larson, Y. Yan and K. Zhu, Surface reaction for efficient and stable inverted perovskite solar cells, *Nature*, 2022, **611**, 278–283.
4 J. Y. Kim, J.-W. Lee, H. S. Jung, H. Shin and N.-G. Park, High-Efficiency Perovskite Solar Cells, *Chem. Rev.*, 2020, **120**, 7867–7918.
5 T. J. Wijaya, S. Xiong, K. Sasaki, Y. Kato, K. Mori, M. Koizumi, S. Lee, M. Kobayashi, Y. Zhou, K. Fukuda, T. Yokota and T. Someya, A Highly Stable Organic–

Inorganic Hybrid Electron Transport Layer for Ultraflexible Organic Photodiodes, *Adv. Mater.*, 2025, 2501951.
6 H. Min, J. Chang, Y. Tong, J. Wang, F. Zhang, Z. Feng, X. Bi, N. Chen, Z. Kuang, S. Wang, L. Yuan, H. Shi, N. Zhao, D. Qian, S. Xu, L. Zhu, N. Wang, W. Huang and J. Wang, Additive treatment yields high-performance lead-free perovskite light-emitting diodes, *Nat. Photonics*, 2023, **17**, 755–760.
7 R. Wang, M. Mujahid, Y. Duan, Z.-K. Wang, J. Xue and Y. Yang, A Review of Perovskites Solar Cell Stability, *Adv. Funct. Mater.*, 2019, **29**, 1808843.
8 S. Sun, M. Lu, X. Gao, Z. Shi, X. Bai, W. W. Yu and Y. Zhang, 0D Perovskites: Unique Properties, Synthesis, and Their Applications, *Adv. Sci.*, 2021, **8**, 2102689.
9 L. Mao, C. C. Stoumpos and M. G. Kanatzidis, Two-Dimensional Hybrid Halide Perovskites: Principles and Promises, *J. Am. Chem. Soc.*, 2019, **141**, 1171–1190.
10 C. Ma, D. Shen, B. Huang, X. Li, W.-C. Chen, M.-F. Lo, P. Wang, M. H.-W. Lam, Y. Lu, B. Ma and C.-S. Lee, High performance low-dimensional perovskite solar cells based on a one dimensional lead iodide perovskite, *J. Mater. Chem. A*, 2019, **7**, 8811–8817.
11 K. Han, J. Jin, B. Su and Z. Xia, Molecular dimensionality and photoluminescence of hybrid metal halides, *Trends Chem.*, 2022, **4**, 1034–1044.
12 J.-Q. Zhao, M.-F. Han, X.-J. Zhao, Y.-Y. Ma, C.-Q. Jing, H.-M. Pan, D.-Y. Li, C.-Y. Yue and X.-W. Lei, Structural Dimensionality Modulation toward Enhanced Photoluminescence Efficiencies of Hybrid Lead-Free Antimony Halides, *Adv. Opt. Mater.*, 2021, **9**, 2100556.
13 S. Smółka, M. Mączka, D. Drozdowski, D. Stefańska, A. Gągor, A. Sieradzki, J. K. Zaręba and M. Ptak, Effect of Dimensionality on Photoluminescence and Dielectric Properties of Imidazolium Lead Bromides, *Inorg. Chem.*, 2022, **61**, 15225–15238.
14 J.-Q. Zhao, H. Ge, Y.-F. Wu, W.-J. Xu, K. Xu, J.-Q. Ma, Q.-L. Yang, C.-Y. Yue and X.-W. Lei, Crystal rigidifying strategy toward hybrid cadmium halide to achieve highly efficient and narrowband blue light emission, *Mater. Today Chem.*, 2022, **24**, 100766.
15 Z. Gan, Y. Cheng, W. Chen, K. P. Loh, B. Jia and X. Wen, Photophysics of 2D Organic–Inorganic Hybrid Lead Halide Perovskites: Progress, Debates, and Challenges, *Adv. Sci.*, 2021, **8**, 2001843.
16 C. C. Stoumpos, D. H. Cao, D. J. Clark, J. Young, J. M. Rondinelli, J. I. Jang, J. T. Hupp and M. G. Kanatzidis, Ruddlesden–Popper Hybrid Lead Iodide Perovskite 2D Homologous Semiconductors, *Chem. Mater.*, 2016, **28**, 2852–2867.
17 M. Ren, S. Cao, J. Zhao, B. Zou and R. Zeng, Advances and Challenges in Two-Dimensional Organic–Inorganic Hybrid Perovskites Toward High-Performance Light-Emitting Diodes, *Nano-Micro Lett.*, 2021, **13**, 163.
18 C. Katan, N. Mercier and J. Even, Quantum and Dielectric Confinement Effects in Lower-Dimensional Hybrid Perovskite Semiconductors, *Chem. Rev.*, 2019, **119**, 3140–3192.
19 C.-J. Que, C.-J. Mo, Z.-Q. Li, G.-L. Zhang, Q.-Y. Zhu and J. Dai, Perovskite-Like Organic–Inorganic Hybrid Lead Iodide with a Large Organic Cation Incorporated within the Layers, *Inorg. Chem.*, 2017, **56**, 2467–2472.
20 Y.-Y. Ma, H.-M. Pan, D.-Y. Li, Y.-H. Liu, T. Lu, X.-W. Lei and Z. Jing, Two-dimensional hybrid halide perovskites composed of mixed corner- and edge-shared octahedron as broadband yellow-light emissions, *Inorg. Chem. Commun.*, 2022, **139**, 109411.
21 A. Yangui, S. Pillet, E.-E. Bendeif, A. Lusson, S. Triki, Y. Abid and K. Boukheddaden, Broadband Emission in a New Two-Dimensional Cd-Based Hybrid Perovskite, *ACS Photonics*, 2018, **5**, 1599–1611.
22 J. Long, Q. Wei, X. Shen, C. Yang, G. Zhang, B. Ke, W. Liang, X. Zhong and B. Zou, Energy Transfer and Self-Trapping Exciton Luminescence in Sb3+-Doped Two-Dimensional Layered Dion–Jacobson Phase Cadmium-Based Perovskites, *J. Phys. Chem. C*, 2024, **128**, 304–314.
23 H.-Y. Hsu, L. Ji, C. Zhang, C. H. Mak, R. Liu, T. Wang, X. Zou, S.-Y. Leu and E. T. Yu, Ultra-stable 2D layered methylammonium cadmium trihalide perovskite photoelectrodes, *J. Mater. Chem. C*, 2018, **6**, 11552–11560.
24 A. Gagor, A. Waskowska, Z. Czapla and S. Dacko, Structural phase transitions in tetra(isopropylammonium) decachlorotricadmate(II), $[(CH_3)_2CHNH_3]_4Cd_3Cl_{10}$, crystal with a two-dimensional cadmium(II) halide network, *Acta Crystallogr., Sect. B*, 2011, **67**, 122–129.
25 W.-Q. Liao, G.-Q. Mei, H.-Y. Ye, Y.-X. Mei and Y. Zhang, Structural Phase Transitions of a Layered Organic–Inorganic Hybrid Compound: Tetra(cyclopentylammonium) Decachlorotricadmate(II), $[C_5H_9NH_3]_4Cd_3Cl_{10}$, *Inorg. Chem.*, 2014, **53**, 8913–8918.
26 M. E. Kamminga, H.-H. Fang, M. R. Filip, F. Giustino, J. Baas, G. R. Blake, M. A. Loi and T. T. M. Palstra, Confinement Effects in Low-Dimensional Lead Iodide Perovskite Hybrids, *Chem. Mater.*, 2016, **28**, 4554–4562.
27 M. D. Smith, B. A. Connor and H. I. Karunadasa, Tuning the Luminescence of Layered Halide Perovskites, *Chem. Rev.*, 2019, **119**, 3104–3139.
28 T. Zhu, W. Weng, C. Ji, X. Zhang, H. Ye, Y. Yao, X. Li, J. Li, W. Lin and J. Luo, Chain-to-Layer Dimensionality Engineering of Chiral Hybrid Perovskites to Realize Passive Highly Circular-Polarization-Sensitive Photodetection, *J. Am. Chem. Soc.*, 2022, **144**, 18062–18068.
29 S. Choi, Y. Li, Y. Kuk and K. M. Ok, $(NH_4)_2Cd_2Cl_3F_3$ and $(NH_4)_2Cd_2Br_3F_3$: The First Fluoride-Containing d10 Metal Mixed Halides Exhibiting Superior Ultraviolet Nonlinear Optical Properties, *Adv. Sci.*, 2025, **12**, 2414503.
30 Y.-Y. Gong, T. Zhang, J. Li, D.-W. Fu, Y. Zhang and H.-F. Lu, Structural Optimization and Property Tunability by Halogen Regulation in Zero-Dimensional Zinc Halide Organic–Inorganic Hybrid Materials, *Cryst. Growth Des.*, 2022, **22**, 6801–6808.
31 K. Kim, Y. Li and K. M. Ok, Hafnium-Based Chiral 2D Organic–Inorganic Hybrid Metal Halides: Engineering Polarity and Nonlinear Optical Properties via Para-

Substituent Effects, *J. Am. Chem. Soc.*, 2025, **147**, 2880–2888.
32 M. Wan, Y.-N. Wang, W.-H. Zhong, H.-R. Chen, Z.-M. Li, C.-H. Shi, Q.-L. Cao, J.-Y. Zhu and L.-Z. Chen, Tuning and Enhancing Nonlinear Optical Behavior in Hybrid Arylammonium Perrhenate Salts through Halogen Substitution, *Chem. Mater.*, 2023, **35**, 8936–8944.
33 Z.-X. Zhang, H. Wang, H.-F. Ni, N. Wang, C.-F. Wang, P.-Z. Huang, Q.-Q. Jia, G. Teri, D.-W. Fu, Y. Zhang, Z. An and Y. Zhang, Organic-Inorganic Hybrid Ferroelectric and Antiferroelectric with Afterglow Emission, *Angew. Chem., Int. Ed.*, 2024, **63**, e202319650.
34 H. F. Zarick, N. Soetan, W. R. Erwin and R. Bardhan, Mixed halide hybrid perovskites: a paradigm shift in photovoltaics, *J. Mater. Chem. A*, 2018, **6**, 5507–5537.
35 M. Karlsson, Z. Yi, S. Reichert, X. Luo, W. Lin, Z. Zhang, C. Bao, R. Zhang, S. Bai, G. Zheng, P. Teng, L. Duan, Y. Lu, K. Zheng, T. Pullerits, C. Deibel, W. Xu, R. Friend and F. Gao, Mixed halide perovskites for spectrally stable and high-efficiency blue light-emitting diodes, *Nat. Commun.*, 2021, **12**, 361.
36 L. Gil-Escrig, C. Dreessen, F. Palazon, Z. Hawash, E. Moons, S. Albrecht, M. Sessolo and H. J. Bolink, Efficient Wide-Bandgap Mixed-Cation and Mixed-Halide Perovskite Solar Cells by Vacuum Deposition, *ACS Energy Lett.*, 2021, **6**, 827–836.
37 Z. Xiao, L. Zhao, N. L. Tran, Y. L. Lin, S. H. Silver, R. A. Kerner, N. Yao, A. Kahn, G. D. Scholes and B. P. Rand, Mixed-Halide Perovskites with Stabilized Bandgaps, *Nano Lett.*, 2017, **17**, 6863–6869.
38 H. Gao, Z. Lu, X. Zhao, K. Zhang, X. Zhu, R. Cheng, S.-L. Li, Z. Qi and X.-M. Zhang, Singlet exciton and singlet/triplet self-trapped excitons for ultra-broadband white-light emission in a zero-dimensional cadmium bromide hybrid, *J. Mater. Chem. C*, 2023, **11**, 9023–9029.
39 C. Sun, Q.-Q. Zhong, X. Zhang, P.-C. Xiao, Y. Cheng, Y.-J. Gao, G.-D. Liu and X.-W. Lei, A Zero-Dimensional Hybrid Cadmium Perovskite with Highly Efficient Orange–Red Light Emission, *Inorg. Chem.*, 2021, **60**, 18879–18888.
40 L.-J. Feng, H.-R. Liu, L.-L. Wang, C.-C. Yang, Y.-W. Ding, X.-W. Lei and Z.-W. Chen, Blue light emissive zero-dimensional hybrid cadmium bromide as fluorescence sensor toward benzaldehyde, *J. Lumin.*, 2024, **270**, 120538.
41 P. Cao, Y.-T. Liu, J.-T. Men, X. Zheng, W. Zhang, L. He and Q. Ye, Dimension-Dependent Phase Transitions, Ferroelasticity, and Photoluminescence in Hybrid Organic–Inorganic Materials, *Inorg. Chem.*, 2023, **62**, 16898–16904.
42 H. Xu, Z. Zhang, X. Dong, L. Huang, H. Zeng, Z. Lin and G. Zou, Corrugated 1D Hybrid Metal Halide [C6H7ClN] CdCl3 Exhibiting Broadband White-Light Emission, *Inorg. Chem.*, 2022, **61**, 4752–4759.
43 S. Siemens, *SAINT, Area-Detector Control and Integration Software*, Siemens Analytical X-ray Instruments Inc., Madison, WI, USA, 1996.
44 R. Blessing, An empirical correction for absorption anisotropy, *Acta Crystallogr., Sect. A: Found. Crystallogr.*, 1995, **51**, 33–38.
45 G. M. Sheldrick, SHELXT–Integrated space-group and crystal-structure determination, *Found. Crystallogr.*, 2015, **71**, 3–8.
46 G. Sheldrick, Crystal structure refinement with SHELXL, *Acta Crystallogr., Sect. C: Struct. Chem.*, 2015, **71**, 3–8.
47 L. Farrugia, WinGX and ORTEP for Windows: an update, *J. Appl. Crystallogr.*, 2012, **45**, 849–854.
48 V. Milman, B. Winkler, J. A. White, C. J. Pickard, M. C. Payne, E. V. Akhmatskaya and R. H. Nobes, Electronic structure, properties, and phase stability of inorganic crystals: A pseudopotential plane-wave study, *Int. J. Quantum Chem.*, 2000, **77**, 895–910.
49 L. Mao, Y. Wu, C. C. Stoumpos, M. R. Wasielewski and M. G. Kanatzidis, White-Light Emission and Structural Distortion in New Corrugated Two-Dimensional Lead Bromide Perovskites, *J. Am. Chem. Soc.*, 2017, **139**, 5210–5215.
50 W. Wang, C.-D. Liu, C.-C. Fan and W. Zhang, Reversible Glass-Crystal Transition in a New Type of 2D Metal Halide Perovskites, *Adv. Funct. Mater.*, 2024, **34**, 2407143.
51 T. Ye, Y. Wang, Z. Gao, S. Ge, H. Qin, X. He, J. Wu, R. Liu, M. Zhu, T. Zhou, Z. Pan, J. Hou, M. Wang, Y. He, L. Wang, H. Chen and W. Jiang, Enhanced Photoluminescence of Cesium Cadmium Chloride via Cu Doping for X-ray Detection and Anticounterfeiting Applications, *ACS Appl. Opt. Mater.*, 2025, **3**, 898–907.
52 Z. Qi, Y. Chen, Y. Guo, X. Yang, F.-Q. Zhang, G. Zhou and X.-M. Zhang, Broadband white-light emission in a one-dimensional organic–inorganic hybrid cadmium chloride with face-sharing CdCl6 octahedral chains, *J. Mater. Chem. C*, 2021, **9**, 88–94.
53 N. Pellet, J. Teuscher, J. Maier and M. Grätzel, Transforming Hybrid Organic Inorganic Perovskites by Rapid Halide Exchange, *Chem. Mater.*, 2015, **27**, 2181–2188.
54 Q. A. Akkerman, V. D'Innocenzo, S. Accornero, A. Scarpellini, A. Petrozza, M. Prato and L. Manna, Tuning the Optical Properties of Cesium Lead Halide Perovskite Nanocrystals by Anion Exchange Reactions, *J. Am. Chem. Soc.*, 2015, **137**, 10276–10281.
55 Y. R. Park, H. H. Kim, S. Eom, W. K. Choi, H. Choi, B. R. Lee and Y. Kang, Luminance efficiency roll-off mechanism in $CsPbBr_{3-x}Cl_x$ mixed-halide perovskite quantum dot blue light-emitting diodes, *J. Mater. Chem. C*, 2021, **9**, 3608–3619.
56 J. Yu, J. Kong, W. Hao, X. Guo, H. He, W. R. Leow, Z. Liu, P. Cai, G. Qian, S. Li, X. Chen and X. Chen, Broadband Extrinsic Self-Trapped Exciton Emission in Sn-Doped 2D Lead-Halide Perovskites, *Adv. Mater.*, 2019, **31**, 1806385.
57 H. Hu, S. A. Morris, X. Qiao, D. Zhao, T. Salim, B. Chen, E. E. M. Chia and Y. M. Lam, Molecular engineering of two-dimensional hybrid perovskites with broadband emission for white light-emitting diodes, *J. Mater. Chem. C*, 2018, **6**, 10301–10307.
58 J.-Y. Liu, M. Zhu, F.-W. Zhang, H.-F. Ni, Z.-L. Li, B. Zhuang, K. Ding, D.-W. Fu, H.-F. Lu and M.-M. Lun, Halogen regulation of multifunctional hybrid materials with photoluminescence and dielectric response, *Inorg. Chem. Front.*, 2024, **11**, 6418–6424.

59 C.-Q. Jing, J. Wang, H.-F. Zhao, W.-X. Chu, Y. Yuan, Z. Wang, M.-F. Han, T. Xu, J.-Q. Zhao and X.-W. Lei, Improving Broadband White-Light Emission Performances of 2D Perovskites by Subtly Regulating Organic Cations, *Chem. – Eur. J.*, 2020, **26**, 10307–10313.

60 Z. Wang, Z. Zhang, L. Tao, N. Shen, B. Hu, L. Gong, J. Li, X. Chen and X. Huang, Hybrid Chloroantimonates(III): Thermally Induced Triple-Mode Reversible Luminescent Switching and Laser-Printable Rewritable Luminescent Paper, *Angew. Chem., Int. Ed.*, 2019, **58**, 9974–9978.